ADVANCED MATERIALS INTERFACES
Open Access
www.advmatinterfaces.de

Niobium-Doped Titanium Dioxide: Effect of Conductivity on Metal-Semiconductor Tribovoltaic Devices

Kaspars Mālnieks, Sabīna Kļimenko, Peter C. Sherrell, Anatolijs Šarakovskis, Raivis Eglītis, Krišjānis Šmits, Artis Linarts, and Andris Šutka**

Tribovoltaic devices have emerged as promising technologies for converting mechanical motion to electricity via surface charge generation. To maximize the electromechanical conversion of tribovoltaic devices, conventional literature has focussed on engineering a large difference in work functions between the contact materials. However, recent reports suggest that other factors beyond work function, such as temperature, play a key role in electromechanical conversion. Herein, TiO_2 (a cheap, abundant oxide material) is doped with Nb^{5+}, resulting in an improved tribovoltaic performance up to 65 times. This is attributed to an enhancement in the TiO_2 film conductivity arising from Nb^{5+} doping. Further, it is shown that this improvement holds over cm^2 scale testing. This work demonstrates the importance of considering a range of factors, particularly conductivity, when designing tribovoltaic devices and may be adopted broadly for optimal electromechanical conversion.

1. Introduction

Tribovoltaic (TV) devices have emerged recently as a pathway to achieve high current devices for mechanical-to-electrical energy conversion. In TV devices, semiconductor-metal or semiconductor-semiconductor junctions move to each other, generating friction between the contacting materials. The form factor of TV devices typically resembles a stylus dragging across a flat surface. The electrical output generated in response to the friction and motion relies on the electronic, mechanical, and topographical properties of each individual and material, leading to diverse studies aimed at increasing electromechanical conversion using a broad set of materials including, p- and n-type silicon,[1] transition metal chalcogenides,[2] metal oxides,[3] and perovskites.[4] One of the key benefits of TV devices in comparison to alternative electromechanical conversion techniques such as piezoelectric or triboelectric nanogenerators is the production of DC current, excluding the need for rectification units, resulting in lower power loss in energy management.

The current density generated by TV devices is highly dependent on the contact area,[3a] with smaller areas creating significantly greater current densities due to tightly confined and localized electric fields. For this reason, TV devices have been shown to create exceeding large current density using ultrafine probes (up to 10^8 A m^{-2}), such as atomic force microscopy tips, yet significantly lower performance using micrometer or millimeter scale interfaces. It is critical to assess these high current densities using nanoscale tips critically, as joule heating would melt even high-temperature ceramics if these currents were to flow through the material at scale. At the large

K. Mālnieks, S. Kļimenko, R. Eglītis, A. Šutka
Institute of Materials and Surface Engineering
Faculty of Natural Sciences and Technology
Riga Technical University
Riga LV-1048, Latvia
E-mail: andris.sutka@rtu.lv

P. C. Sherrell
School of Science
RMIT University
Melbourne 3000, Australia
E-mail: peter.sherrell@rmit.edu.au

A. Šarakovskis, K. Šmits
Institute of Solid State Physics
University of Latvia
Riga LV-1063, Latvia

K. Šmits
Institute of Biomaterials and Bioengineering
Faculty of Natural Sciences and Technology
Riga Technical University
Riga LV-1048, Latvia

A. Linarts
Institute of Technical Physics
Faculty of Natural Sciences and Technology
Riga Technical University
Riga LV-1048, Latvia

The ORCID identification number(s) for the author(s) of this article can be found under https://doi.org/10.1002/admi.202400567

DOI: 10.1002/admi.202400567

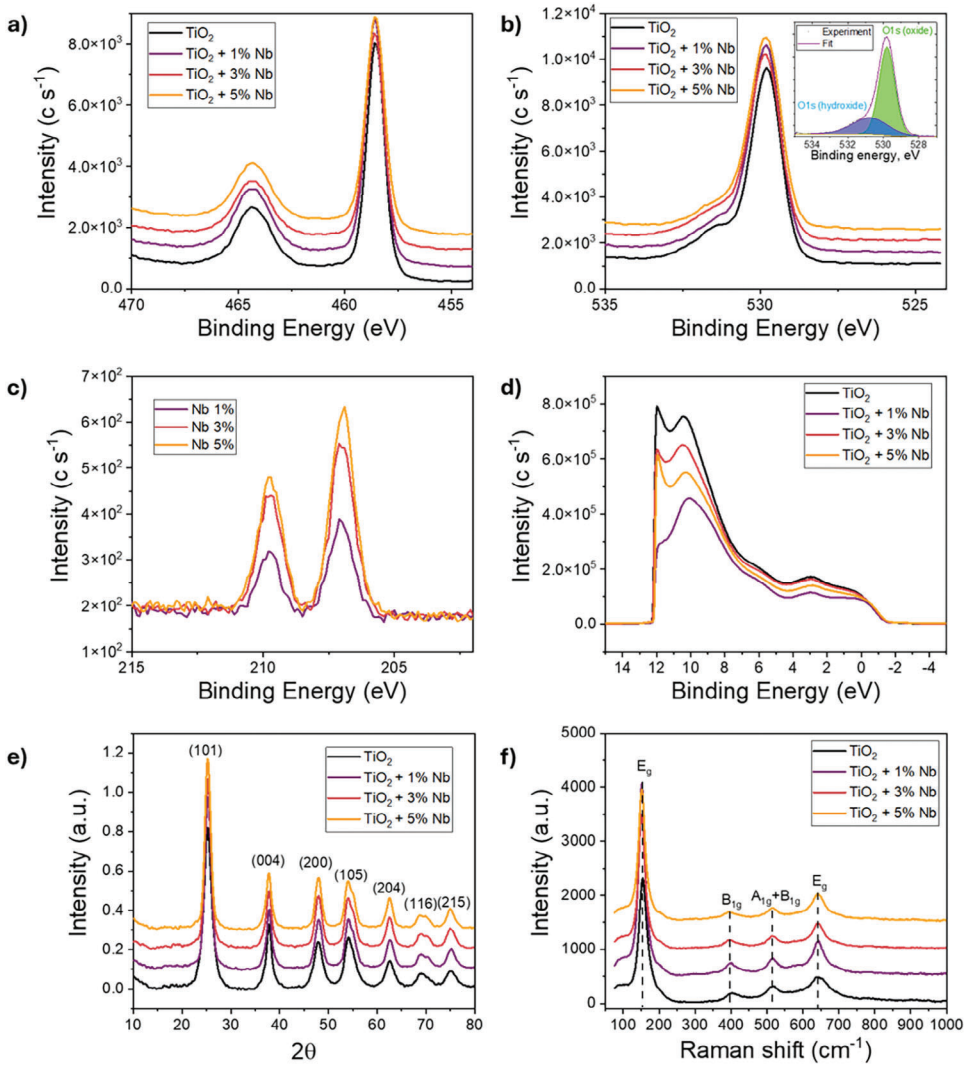

Figure 1. Electronic, Chemical, and Crystal Characterization of Nb-TiO_2 films with 0–5 at% of Nb content, a–c) core level X-Ray Photoelectron Spectroscopy showing, a) Ti 2p peaks, b) O 1s peaks, c) Nb 3d peaks, d) UV Photoelectron spectroscopy, e) X-ray diffraction, and f) Raman spectroscopy.

(herein defined as millimeter) scale, contact area the most impressive output to date was provided by Zhang et al,[5] generating a power density of 11.85 W m^{-2} and an energy density of 9.23 W m^{-2} from sliding contact between p-type Bi_2Te_3 versus n-type GaN.[5]

Whilst research on TV devices is progressing rapidly, the underlying mechanisms remain open for debate, with dynamic junction,[6] hot electron injection,[3b] and/or the thermoelectric effect all being demonstrated to play key roles in different material combinations.[3a]

One of the key challenges is unlocking the potential of TV devices, is in choosing the correct material pair with the desired electronic properties. When considering the use of these devices in practical applications, low-cost, highly chemically and mechanically stable, materials are coveted. As one of the world's most abundant materials, titanium dioxide, TiO_2, has shown great promise across a broad range of energy applications, due to excellent charge transport properties,[7] including super capacitive energy storage,[8] photocatalysis,[9] water electrolysis,[10] and recently for TV devices.[3a] As a cheap, abundant semiconductor it is imperative to develop a clear understanding of how TiO_2 can be exploited for diverse applications including TV devices. TiO_2 is also an attractive material as it can be easily doped with a range of elements and compounds to alter its optoelectronic properties to achieve target performance.[11] Recently, Nb-doped TiO_2 has received scientific and technological interest due to its promising electrical and optical properties.[12] Specifically, it has been proposed not only as a potential low-cost alternative to such popular conducting oxides as Sn-doped In_2O_3[13] and F-doped SnO_2[14] but also as a key to improved dye-sensitized solar cells[15] and for applications in photocatalysis[16] and photochromic devices.[17] However, despite these exceptionally promising optoelectronic properties, along with excellent thermal and long-term chemical stability up to 700 °C,[18] the TV performance of Nb-TiO_2 remains unexplored.

Herein, we test the effect of modulating the chemistry and electronic properties of TiO_2, via doping with Niobium, Nb. Nb was selected as it does not significantly affect TiO_2 crystal

Table 1. Stoichiometry of Nb-TiO_2 samples calculated from XPS fitting.

	Ti	O (oxide)	O (OH)	Nb	S	Nb/Ti	Ti/O (oxide)	Ti/O (total)
TiO_2 0% Nb	29.30	53.65	15.39	0.00	1.67	0.000	0.546	0.424
TiO_2 1% Nb	29.72	47.14	21.21	0.60	1.33	0.020	0.630	0.435
TiO_2 3% Nb	27.95	47.44	22.05	1.20	1.37	0.043	0.589	0.402
TiO_2 5% Nb	28.80	48.16	20.47	1.37	1.20	0.048	0.598	0.420

structure, enabling the production of small nanoparticles without altering the produced TiO_2 phase. TiO_2 films with Nb:Ti ratios ranging from 0.020 to 0.048 were produced, and their performance was probed against Nickel, Copper, or Zinc coated on carbon felts TV devices. The optimal Nb-TiO_2 (Nb:Ti = 0.020) sample demonstrated an 800% improvement in the current generated compared to pure TiO_2 films. This work provides a simple pathway for improving the output of semiconductor-based TV devices.

2. Results and Discussion

TiO_2 and Nb-TiO_2 nanoparticles were produced by a method described by *Scolan* and *Sanchez*,[19] with films produced on FTO glass via spin coating and subsequent heat-treatment (see experimental section for full details).

2.1. Elucidating the Electronic, Chemical, and Physical Properties of Nb-TiO2

To confirm the composition and stoichiometry of the produced samples, XPS analysis was performed (**Figure 1**a–d). X-ray photoelectron spectroscopy (XPS) revealed the clear presence of Ti^{4+} (the peak of Ti 2p located at 458.5 eV, Figure 1a)[20] and Nb^{5+} (the peak of Nb 3d is located at 207.0 eV, Figure 1c).[21] The O 1s region contains 2 peaks located at 529.8 and 530.8 eV corresponding to lattice oxygen and surface-adsorbed oxygenated species, such as —OH and H_2O,[20] respectively (Figure 1b). The atomic compositions of the produced materials were assessed with respect to the precursor atomic percent of Nb, ranging from 0 at% (Figure S1, Supporting Information) to 5 at% (Figure 1c and **Table 1**).

The XPS data shows that in all cases, the produced TiO_2 samples are oxygen deficient, and the Nb:Ti ratio ranged from 0.020 to 0.048 (for 1 at% precursor, and 5 at% precursors respectively). The presence of sulfur (Figure S2, Supporting Information) in the films arises from a residual trace amount of sodium dodecyl sulfate from the surfactant used in the particle synthesis process.[22] The authors note that the at% precursors relate to the atomic percentage of Nb added to Ti, excluding oxygen and ligands. Energy dispersive X-ray spectroscopy of the films showed 1.17 at% Nb, 2.77 at% Nb, and 4.84 at% Nb when only considering Titanium and Niobium, corresponding to 1 at % Nb, 3 at% Nb and 5 at% Nb compositions respectively.

The work function (WF) of the Nb-TiO_2 samples was determined by ultraviolet photoelectron spectroscopy (UPS) (Figure 1d) using the method described by Klein.[23] The work function values were consistently measured to be ≈4.0 eV across various samples, with variations falling within experimental error. To further probe this, Ar+ etching was performed to remove the layer of adventitious carbon (Figure S3, Supporting Information). For the duration of etching (up to 45 s), there was only incomplete removal of the adventitious carbon layer, however, further etching was not performed as an additional band in the spectrum of Ti spectra at 458 eV was observed to appear after etching. This peak is representative of the reduction of Ti^{4+} to Ti^{3+} and the formation of TiO_{2-x} (Figure S4, Supporting Information), indicating that the etching process is altering the Nb-TiO_2 samples significantly. Thus, while the values of the WF of the samples after the cleaning increased (Figure S5 and Table S1, Supporting Information) this cannot be correlated with the presence of Nb in the samples.

To probe the crystal phase of the produced materials X-ray diffraction (XRD) (Figure 1e) and Raman spectroscopy (Figure 1f) were performed. According to XRD all of the samples can be attributed to single-phase anatase TiO_2 (JCPDS 21-1272).[24] The crystallinity of the samples was found to decrease from 94.8% for 0% Nb-TiO_2 to 87.7%, 82.1% and 83.5% for 1, 3, and 5 at% Nb-TiO_2, respectively.

Raman spectroscopy (Figure 1f) confirmed the anatase crystal structure of the Nb-TiO_2 samples. For the un-doped TiO_2 nanoparticles, the band positions were 154, 402, 516, and 642 cm^{-1}, for the E_g, B_{1g}, A_{1g}+B_{1g}, and the secondary E_g band, respectively. These slight red-shifts compared to standard peak positions arise from the small size (< 10 nm diameter) of the nanoparticles (Figure S6, Supporting Information).[25] The addition of Nb^{5+} caused a slight shift of the main E_g band (from 154 to 152 cm^{-1}) due to the presence of Nb—O—Ti bonds.[26]

With a clear understanding of the composition and structure of the produced Nb—TiO_2 samples, the samples were assessed for their tribovoltaic performance, which is described in the subsequent section.

2.2. Tribovoltaic Performance of Nb-TiO_2 Films

The Nb-TiO_2 films were analyzed via cross-sectional scanning electron microscopy (SEM) with the annealed films showing a range of thickness of 720 ± 30, 640 ± 50, 710 ± 40, and 760 ± 20 nm for 0, 1, 3, and 5% Nb respectively (**Figure 2**).

To test the tribovoltaic performance of the produced films on a large scale, carbon felt (CF) was coated with Ni, and a 1 cm^2

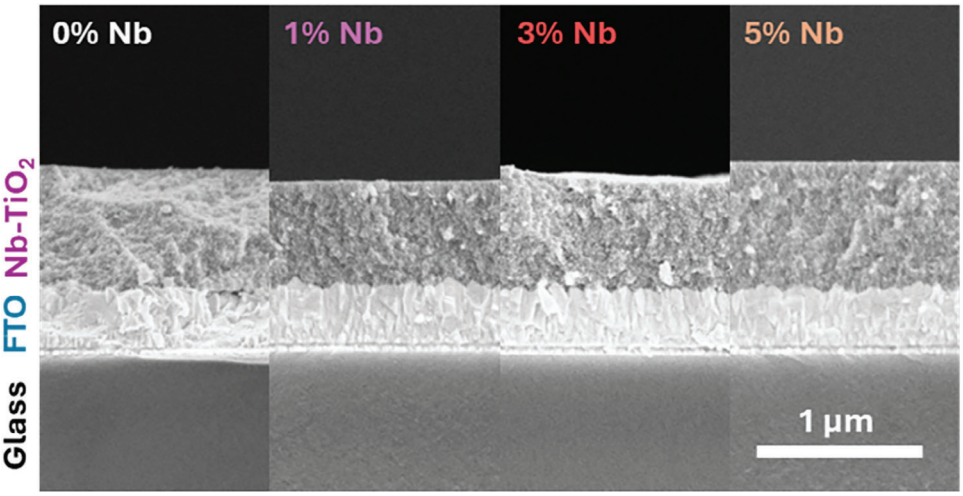

Figure 2. Cross-sectional SEM of annealed Nb-TiO_2 samples.

area of this coated felt was slid over the surface of the films with the resultant current measured (schematically represented in **Figure** 3a). When the Ni-CF contact was rubbed against "as-deposited" Nb-TiO_2 films, minimal change in output current was observed, with all samples showing a current between 1.1 and 1.4 nA (Figure 3b). This is attributed to the as deposited films having a heterogenous, inconsistent structure. In contrast, the annealed Nb-TiO_2 films showed an order of magnitude higher current, with the 0 at% TiO_2 film increasing in TV current generation from 1.28 to 12 nA, a 15-fold improvement (Figure 3c).

The fluctuation (or spikes) in current (Figure 3b,c) throughout the TV measurement has not been explored in detail in the literature, however, it is generally considered that these features arise from the sliding probe (in this case the foam) becoming "stuck" (lowering the current) and then overcoming this "stuck" component releasing significantly greater energy than continuous motion.[27]

Critically, the annealing process resulted in homogenous films (as seen in Figure 2), which enabled the effect of Nb doping to be observed whilst excluding topographical effects. Here, a marked increase in TV current generated for all Nb-containing TiO_2 films was observed, with a maximum current of 83 nA for the 1 at% Nb-TiO_2 samples (Figure 3c,d). This represents a 65-fold increase in current compared to the as-deposited undoped TiO_2 (Figure 3e), and 7-fold increase compared to annealed undoped TiO_2. With a continued increase in Nb content, the TV current stabilizes at 30 nA, still 2.5 times higher than undoped annealed TiO_2.

In the common interpretation of TV phenomena, the difference in work function between the two contact surfaces is attributed as the main driving force for the generated current. However, as shown via UPS spectroscopy (Figure 1d) there is minimal change in the work-function of the Nb-TiO_2 films regardless of Nb content (Table S1, Supporting Information). Therefore, the enhancement of TV current with the addition of Nb cannot be related to the change of work function.

The best understanding of what causes the TV effect is the charge depletion mechanism. The charge depletion mechanism describes the formation of a charge depletion layer at the junction between the semiconductor and metal. During the friction and sliding, the depletion layer disappears at the rear side of the metal electrode and is re-established in the direction of motion. The difference between the rate of depletion layer formation and destruction breaks the equilibrium between the charge carrier distribution at the junction. This broken equilibrium leads to current generation due to the acceleration of the in-built electric field.[6] When factors that influence the charge depletion mechanism are considered, the ability of the material to conduct these charges is a key parameter. In Nb-TiO_2 samples, the Nb^{5+} acts as a substitutional donor dopant in the Ti^{4+} lattice, thus to maintain electroneutrality in the crystal lattice, point defects are formed (Figure S8, Supporting Information), such as Ti^{3+} or delocalized electrons.[28] Both of these effects enhance the electric conductivity of the TiO_2. However, the increased electrical conductivity is counter balanced by the slightly larger Nb^{5+} cations (compared to the Ti^{4+} cations) acting as scattering centres for charge carriers. This balance between enhanced conductivity and charge carrier scattering explains why the current is increased significantly for the 1 at% Nb-TiO_2 sample (0.02 Nb:Ti ratio). To confirm this, resistivity measurements on the films were performed using the Standard Methods of Testing for Electrical Resistance of Insulation Materials, ASTM Designation D257-14. The resistivity was measured to be 4.5×10^{15}, 5.5×10^{13}, 3.3×10^{9}, and 2.1×10^{10} Ω cm for TiO_2, 1, 3, and 5 at% Nb respectively, as a control a glass slide was measured to have a resistivity of 6.2×10^{15} Ω cm. These results suggest there is a balance between charge carrier concentration, charge mobility, and electrical conductivity which may provide future insights into fundamental TV phenomenon. In energy harvesting and conversion materials, such an interplay between carrier concentration and conductivity is also observed in thermoelectric materials, where increasing conductivity increases the thermoelectric figure of merit, but decreases the Seebeck coefficient, leading to there being an optimal range of carrier concentration, electrical conductivity, and thermal conductivity.[29] This suggests that in the future, as the TV field matures, there is a need to define a TV figure of merit that can mathematically express this balance of material properties to enable precise design of optimal TV materials.

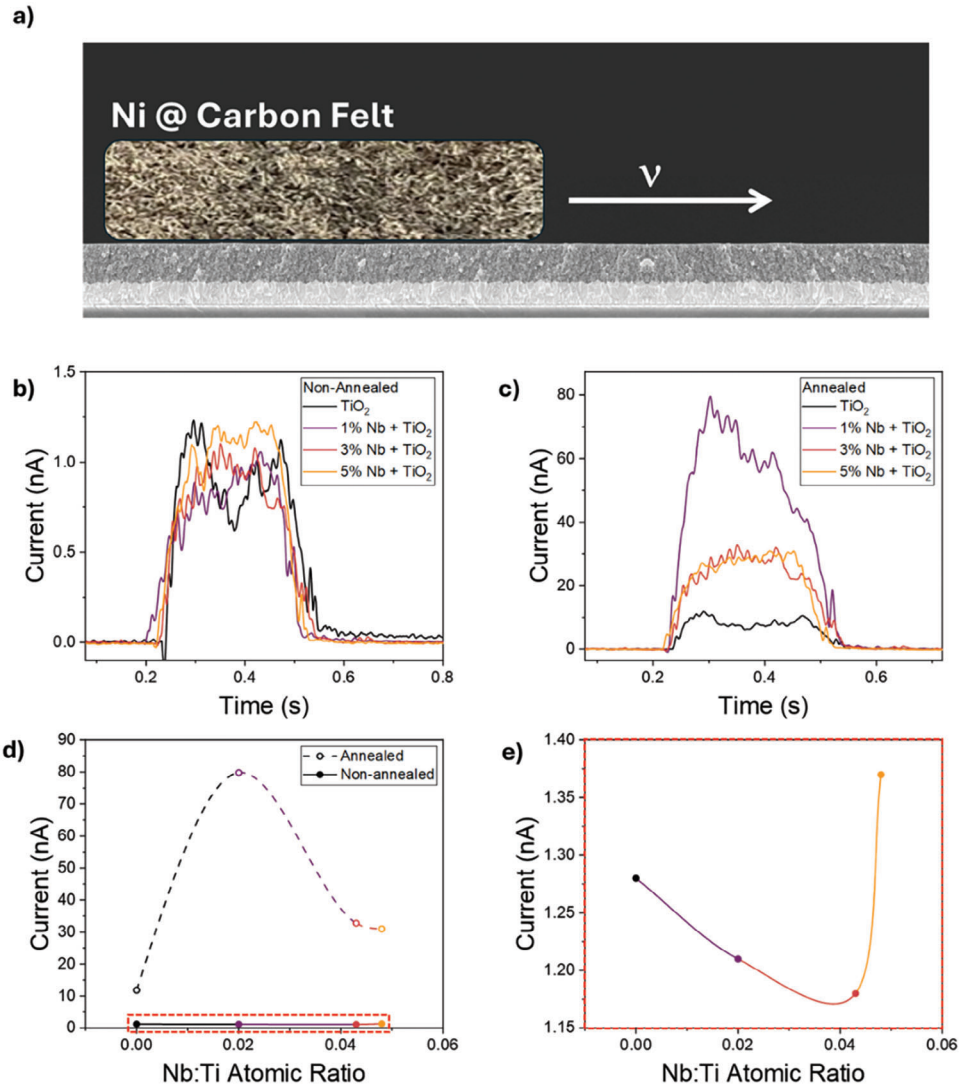

Figure 3. Assessment of the effect of Nb content on tribovoltaic performance, a) Schematic of the large area testing set up using metal-coated carbon felts, b) measured current over time as a Ni felt moved across as deposited (non-annealed) Nb-TiO_2 samples at a speed of 20 mm s^{-1} and a constant force of 0.3 N, b) the current generated under equivalent conditions from annealed Nb-TiO_2 films, d) generated maximum current at different Nb: Ti ratios, and e) expansion of the non-annealed film region from d.

The effect of sliding speed and force is demonstrated in Figure S7 (Supporting Information). With increasing sliding speed (from 0.7 to 2.0 cm s^{-1}) and force (from 0.1 to 0.3 N), the current increases. These results are in line with previous literature,[1b,30] and serve to demonstrate the reliability of the results.[4] At 2.0 cm s^{-1}, the sliding distance was ≈0.6 cm, decreasing to ≈0.35 cm at 0.7 cm s^{-1}.

To probe the role of different metal contacts on the 1 at% Nb-TiO_2 films, Zn, Cu, and Ni were separately deposited on carbon felts (**Figure** 4a; Figure S9, Supporting Information). These metals were chosen due to their distinct work functions (3.63, 4.53, and 5.22 eV) falling on either side of the work-function of the Nb-TiO_2 samples. While TV devices typically show relatively high current values compared to other electromechanical conversion technologies, this comes with lower voltages. In the Nb-TiO_2 device in contact with Ni foil, the maximum measured voltage was 0.26 V (260 V m^2, Figure S10, Supporting Information) corresponding to a power and energy of 17.8 pJ (0.178 mJ m^{-2}) and 27.6 pW (0.276 mW m^{-2}) respectively.

The measured maximum current for 1 at% Nb-TiO_2 in contact with Zn, Cu, Ni, and C felts was measured to be 58.9, 29.11, 79.88, and 20.3 nA respectively (Figure 4b,c). However, there was no correlation between either work-function (Figure 4d) or work-function difference (Figure 4e) with the measured charge – which is in line with prior reports for TiO_2 TV devices. Here, the bigger difference in electromechanical conversion may arise from the quality of the metal coating of the carbon felt (Figure S9, Supporting Information), rather than the electronic interactions. The low measured current (maximum current density of 0.78 mW m^{-2}) from the uncoated carbon felt suggests that in these large-scale testing, the conductivity and delocalized electrons from metallic systems are needed to observe a significant TV effect.

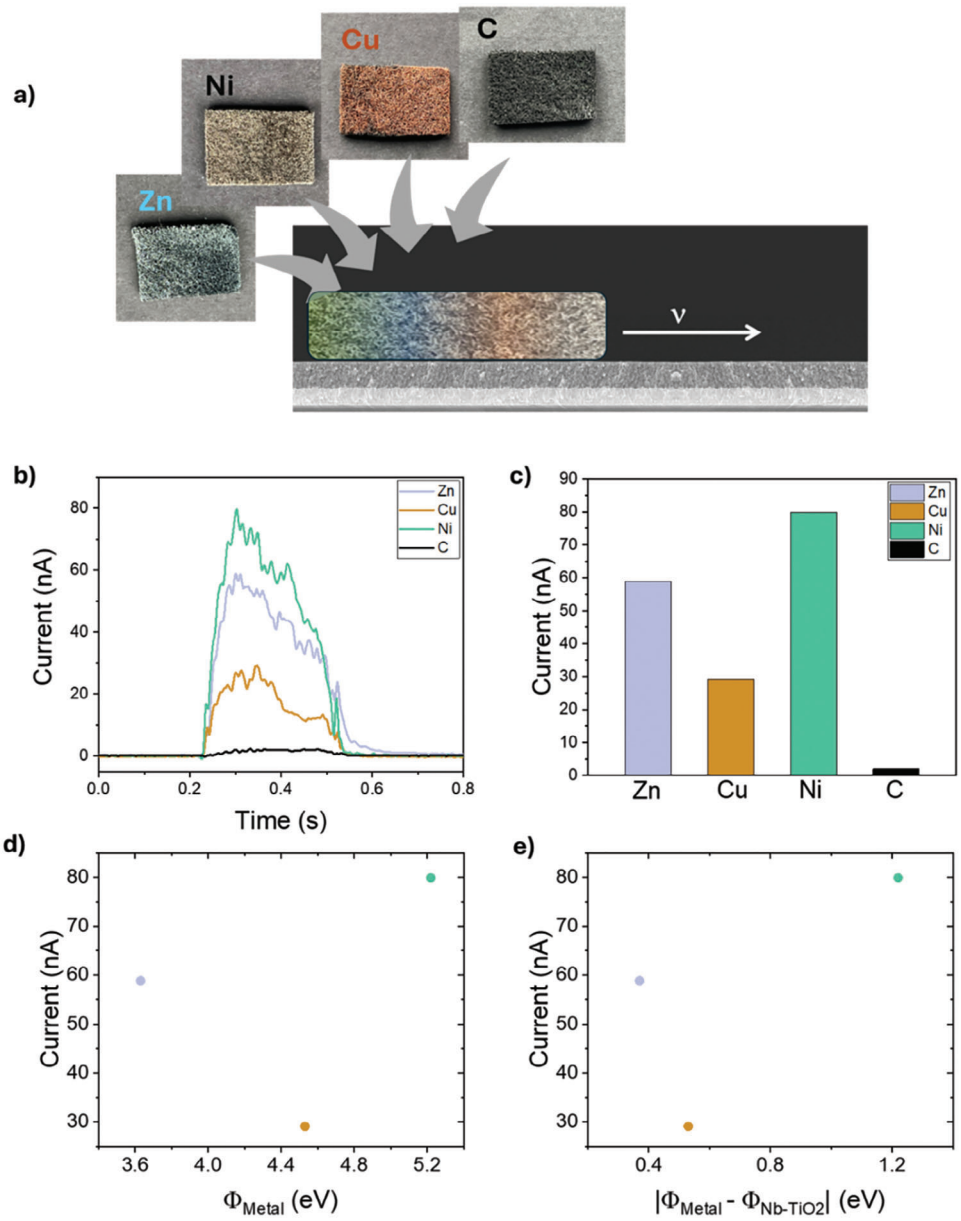

Figure 4. Tribovoltaic performance of 1 at% Nb-TiO_2 in contact with different metals, a) schematic of the testing process, b) raw current curves for contact with Zn, Cu, Ni, and C, c) maximum currents obtained from (b), d) influence of metal work-function on measured current, and e) influence of the difference in work function between 1 at% Nb-TiO_2 and the contact metal.

Prior literature has reported TV device output current to be dependent on the metal work function, with the key parameter being the difference in work function between the metal and semiconductor (a larger difference in work function increases the built-in electric field).[30b] On the other hand, for TV metal-TiO_2 sliding junctions the current density has been reported to show little correlation with the work function of the contact metal and a strong correlation with the contact area.[3a]

The role of friction on charge generation and thermal charge transport is schematically demonstrated in **Figure 5**. Conceptually, a smaller probe size leads to a greater thermal gradient, and also a shorter distance for surface charges to travel when excited by friction, leading to higher measured electrical outputs. Such concepts, may explain lower outputs in multi-probe or multi-friction interface scaling of TV devices, where multiple friction points lower the thermal gradient and thus decrease thermoelectric charge generation and also thermally driven surface charge flow.

Based on these results, the Nb-TiO_2 films were subjected to over 1000 cycles with the Ni-coated carbon felt (**Figure 6**; Figure S11, Supporting Information). The film showed remarkable wear resistance, as expected from the materials excellent thermal and chemical stability,[18] with no appreciable change in produced current over the 1000 cycles. Examination of the contact surface

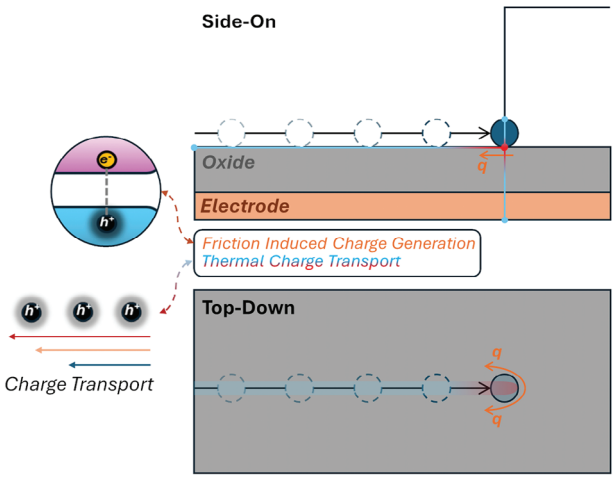

Figure 5. The combined influence of frictional charge generation and thermoelectric or thermally enhanced charge transport on tribovoltaic devices.

of the Nb-TiO_2 surface showed no degradation or wear, indicating that the current generation would be stable over practical device lifetimes.

3. Conclusion

Titanium dioxide films doped with Nb at varied concentrations were produced via spin coating of nanoparticles. The addition of just 1 at% of Nb precursor into the TiO_2 film led to a 65-fold increase in tribovoltaic current (compared to an equivalent TiO_2 film) when in contact with a 1 cm^2 Ni-coated carbon felt. Contrary to the current understanding from the field, this enhancement is attributed to an improvement in film conductivity rather than any effect of work-function. The produced films show exceptional stability over 1000 cycles of tribovoltaic testing, highlighting the potential future practical use of such materials and devices.

4. Experimental Section

Particle Synthesis: The nanoparticles used in this research were synthesized via a sol–gel synthesis first described by *Scolan* and *Sanchez*[19] that was further modified to allow for the preparation of doped TiO_2 nanoparticles. In a typical synthesis procedure, 9.05 mL titanium tetra n-butoxide (97%, Sigma–Aldrich) was added to a mixture of 8.268 mL acetylacetone (99.0%, Merck) in 12.36 mL *n*-Butanol (99.5%, Merck, dried over CaH_2). Afterward, a mixture of niobium ethoxide (99.95%, Sigma–Aldrich) in a similar mixture of acetylacetone and *n*-butanol was added to this titania precursor solution. This was done under nitrogen gas flow. The amount of niobium ethoxide was dependent on the desired doping level. The amount of acetylacetone and n-Butanol was the same molar ratio as was for the titanium precursor solution. Afterward, the solution was brought up to reflux and a mixture of 1.76 g 4-dodecylbenzene sulfonic acid (95%, Sigma–Aldrich) in 4.86 mL of deionized water was added dropwise to the metal precursor solution. All of this was kept under reflux for 12 h. This was followed up by transferring the solution to a Teflon lined autoclave and solvothermally treated for 24 h at 150 °C. The synthesized nanoparticles were separated and washed twice with methanol via centrifugation 2000 g for 1 h. Finally, the particles were dispersed in *N*, *N*-dimethylformamide, at a concentration of 100 g L^{-1}.

Preparation of TiO_2 Films and Sliding Electrodes: The nanoparticles were stripped from the surfactant coating via chemical stripping. For this to the Nb-doped TiO_2 nanoparticle colloid in DMF, toluene was added in a ratio of 2:1 to DMF followed by further addition of 2 mass equivalents of Nitrosyl tetra fluoro borate in dichloromethane. Afterward, the particles were washed with water and methanol via centrifugation at 2000 g for 20 min and finally dispersed in DMF for a concentration of 100 g L^{-1}.

The films were prepared via spin coating unto air plasma pre-treated fluorine-doped tin oxide (FTO) glass substrates by dynamically coating the samples at 5000 rpm for 30 s. Afterward, the samples were dried at 150 °C for 1 h. For the samples that were heat treated, calcination at 400 °C for 2 h was done.

Characterization Techniques: Transmission Electron Microscopy (TEM): The verification of crystalline size and morphology studies of nanoparticles were conducted using a transmission electron microscope (TEM, Tecnai G2 F20, FEI) operating at 200 kV. Samples for TEM analysis were prepared on 3 nm carbon-coated holy carbon grids (AGS186-4, Agar Scientific).

Scanning Electron Microscopy (SEM): The morphology of layers was investigated using a high-resolution SEM-FIB electron microscope, Helios 5 UX (Thermo Scientific), operating at 2 kV and equipped with a TLD (Thrulens SE detector). For determining layer thickness, a focused ion beam (FIB) cross-section was initially performed. However, subsequent analysis using a simple sample broken revealed finer details and grain structure. Since both methods yielded consistent thickness results, the breaking approach was adopted for all samples. Quantitative analysis was carried out using the Oxford Aztec X-Max 150 energy dispersive X-ray spectrometer (EDS). To ensure accuracy, the analysis focused solely on the Nb concentration in relation to Ti, excluding elements from the substrate and other layers.

Photoelectron Spectroscopy: X-ray photoelectron spectroscopy (XPS) and UV photoelectron spectroscopy (UPS) analyses were used to characterize the materials. The XPS measurements were carried out using a ThermoFisher ESCALAB Xi+ instrument using a monochromatic Al Kα X-ray source. The calibration of the binding energy scale is confirmed by examining the sputter-cleaned Au, Ag, and Cu reference samples that place Au $4f_{7/2}$, Ag $3d_{5/2}$, and Cu $2p_{3/2}$ peaks at 83.96, 368.21, and 932.62 eV, respectively. The charge neutralizer was not used in the reported experiments. The spectra were recorded using an X-ray beam size of 650 × 100 µm with a pass energy of 20 eV and a step size of 0.1 eV. Data from all materials have been referenced using the main signal of the carbon 1s spectrum assigned to occur at 284.8 eV. The carbon 1s spectrum was collected using high-energy resolution settings. The same instrument was used for UPS measurements with unmonochromatized He I radiation ($h\nu = 21.22$ eV). To collect a reliable electron signal, a negative bias voltage (up to −5 V) has been applied to the samples. A standard procedure was used in which the WF is assessed by a linear extrapolation of the low-kinetic energy electron tail toward the BE axis.

X-Ray Diffraction (XRD): Dried nanoparticles were characterized via XRD (*PANalytical X'Pert*) using Cu Kα radiation and Raman spectroscopy (*Renishaw inVia*) using a laser with a wavelength of 532 nm to determine their composition as well as crystallinity and to ascertain whether or not doping has been successful.

Electrical Measurements: Tribovoltaic performance measurements were carried out using a sliding rail-based control system to control the horizontal movement of the TiO_2 thin films. The sample was fixed on a platform that was able to travel in a horizontal direction along the axis of the rail. The metal felts with a 1 cm^2 geometric area were attached to a cantilever fixed to the Zwick/Roell Z2.5 material testing machine, which controlled the distance and force between the metal felt and TiO_2 thin film. Under the control of a microcontroller unit and computer, the sliding rail moved horizontally at a constant speed. The pressure and speed can slightly change with a variation of 10% due to inherent mechanical errors, such as the flatness of the mechanical arm and frame. Current measurements were recorded with a Keithley 6514 electrometer connected to a PicoScope 5444B PC oscilloscope to provide high-time resolution.

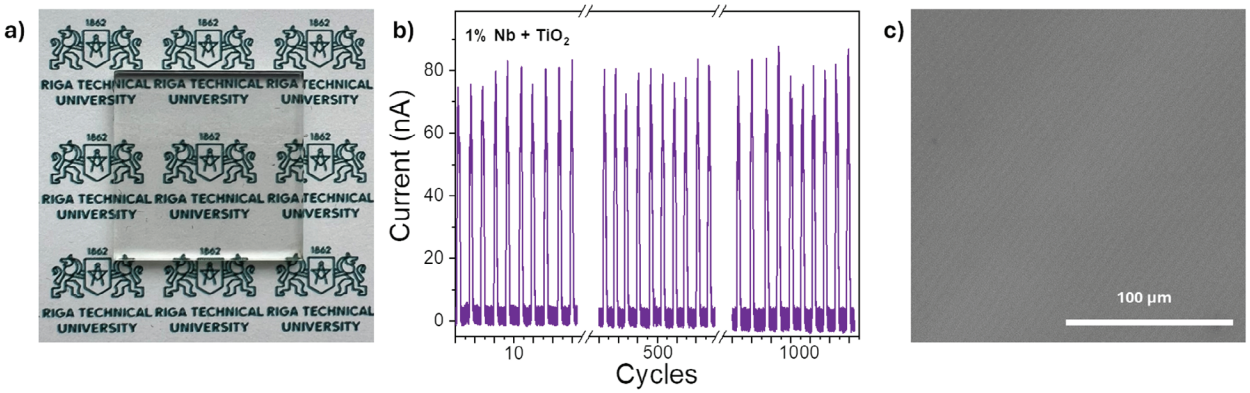

Figure 6. Tribovoltaic stability testing of 1 at% Nb-TiO_2 films, a) photo of the 1 at% Nb-TiO_2 film, b) Stability over > 1000 cycles at 2 cm s^{-1} sliding speed, and c) top-down SEM image of the surface after 1000 cycles showing no significant degradation.

Resistivity measurements are based on the ASTM standard of the American Society for Testing and Materials, specifically, the Standard Methods of Test for Electrical Resistance of Insulation Materials, ASTM Designation D257-14, using the Keithley 8009 resistivity test fixture coupled with the Keithley 6517b electrometer.

Supporting Information

Supporting Information is available from the Wiley Online Library or from the author.

Acknowledgements

The authors would like to acknowledge the Latvian Research Council in the frame of the project "Engineering of dynamic Schottky diode generators based on wide band gap semiconductors and hot electron injection" (grant no. lzp-2021/1- 0129). P.C.S. acknowledges support from the RMIT Vice-Chancellors Research Fellowship Scheme (2023).

Open access publishing facilitated by RMIT University, as part of the Wiley - RMIT University agreement via the Council of Australian University Librarians.

Conflict of Interest

The authors declare no conflict of interest.

Data Availability Statement

The data that support the findings of this study are available from the corresponding author upon reasonable request.

Keywords

energy harvesting, metal-semiconductor junction, niobium, titanium dioxide, tribovoltaic

Received: June 28, 2024
Revised: July 31, 2024
Published online: August 15, 2024

[1] a) J. Liu, M. Miao, K. Jiang, F. Khan, A. Goswami, R. McGee, Z. Li, L. Nguyen, Z. Hu, J. Lee, K. Cadien, T. Thundat, *Nano Energy* **2018**, *48*, 320; b) S. Lin, R. Shen, T. Yao, Y. Lu, S. Feng, Z. Hao, H. Zheng, Y. Yan, E. Li, *Adv. Sci.* **2019**, *6*, 1901925.
[2] J. Liu, F. Liu, R. Bao, K. Jiang, F. Khan, Z. Li, H. Peng, J. Chen, A. Alodhayb, T. Thundat, *ACS Appl. Mater. Interfaces* **2019**, *11*, 35404.
[3] a) A. Sutka, K. Mālnieks, M. r. s. Zubkins, A. r. Plūdons, A. Sarakovskis, O. Verners, R. Eglītis, P. C. Sherrell, *ACS Appl. Mater. Interfaces* **2023**, *15*, 33140; b) A. Sutka, M. Zubkins, A. Linarts, L. Lapčinskis, K. Mālnieks, O. Verners, A. Sarakovskis, R. Grzibovskis, J. Gabrusenoks, E. Strods, *J. Phys. Chem. C* **2021**, *125*, 14212.
[4] Z. Hao, T. Jiang, Y. Lu, S. Feng, R. Shen, T. Yao, Y. Yan, Y. M. Yang, Y. Lu, S. Lin, *Matter* **2019**, *1*, 639.
[5] Z. Zhang, Z. Wang, Y. Chen, Y. Feng, S. Dong, H. Zhou, Z. L. Wang, C. Zhang, *Adv. Mater.* **2022**, *34*, 2200146.
[6] Y. Lu, Z. Hao, S. Feng, R. Shen, Y. Yan, S. Lin, *iScience* **2019**, *22*, 58.
[7] X. Sheng, D. He, J. Yang, K. Zhu, X. Feng, *Nano Lett.* **2014**, *14*, 1848.
[8] X. Lu, G. Wang, T. Zhai, M. Yu, J. Gan, Y. Tong, Y. Li, *Nano Lett.* **2012**, *12*, 1690.
[9] Q. Guo, C. Zhou, Z. Ma, X. Yang, *Adv. Mater.* **2019**, *31*, 1901997.
[10] M. Iesalnieks, M. Vanags, L. L. Alsina, R. Eglītis, L. Grinberga, P. C. Sherrell, A. Sutka, *Adv. Sci.* **2024**, *11*, 2401261.
[11] a) N. Boonprakob, N. Wetchakun, S. Phanichphant, D. Waxler, P. Sherrell, A. Nattestad, J. Chen, B. Inceesungvorn, *J. Colloid Interface Sci.* **2014**, *417*, 402. b) A. Zaleska, *Recent patents on engineering* **2008**, *2*, 157. c) Y. C. Nah, I. Paramasivam, P. Schmuki, *Chem. Phys. Chem.* **2010**, *11*, 2698.
[12] K. Safeen, V. Micheli, R. Bartali, G. Gottardi, A. Safeen, H. Ullah, N. Laidani, *Mater. Sci. Semicond. Process.* **2017**, *66*, 74.
[13] A. Manole, M. Dobromir, M. Girtan, R. Mallet, G. Rusu, D. Luca, *Ceram. Int.* **2013**, *39*, 4771.
[14] L. De Trizio, R. Buonsanti, A. M. Schimpf, A. Llordes, D. R. Gamelin, R. Simonutti, D. J. Milliron, *Chem. Mater.* **2013**, *25*, 3383.
[15] B.-R. Koo, D.-H. Oh, H.-J. Ahn, *Appl. Surf. Sci.* **2018**, *433*, 27.
[16] S. Khan, H. Cho, D. Kim, S. S. Han, K. H. Lee, S.-H. Cho, T. Song, H. Choi, *Appl. Catal., B* **2017**, *206*, 520.
[17] R. Eglītis, U. Joost, A. Zukuls, K. Rubenis, R. Ignatāns, L. g. Avotiņa, L. Baumane, K. n. Šmits, M. Hirsimäki, T. Käämbre, A. Šutka, *ACS Appl. Mater. Interfaces* **2020**, *12*, 57609.
[18] Y. Gao, Y. Liang, S. A. Chambers, *Surf. Sci.* **1996**, *365*, 638.
[19] E. Scolan, C. Sanchez, *Chem. Mater.* **1998**, *10*, 3217.
[20] B. Zeng, S. Wang, Y. Gao, G. Li, W. Tian, J. Meeprasert, H. Li, H. Xie, F. Fan, R. Li, C. Li, *Adv. Funct. Mater.* **2021**, *31*, 2005688.
[21] B. Boruah, R. Gupta, J. M. Modak, G. Madras, *Nanoscale Advances* **2019**, *1*, 2748.

[22] C. D. Wagner, *NIST Standard Reference Database Number* **2000**, *20*, https://srdata.nist.gov/xps/SpectralByCompdDd/25793 (accessed: August 2024).
[23] A. Klein, *J. Am. Ceram. Soc.* **2013**, *96*, 331.
[24] X. Wei, G. Zhu, J. Fang, J. Chen, *Int. J. Photoenergy* **2013**, *2013*, 726872.
[25] W. Zhang, Y. He, M. Zhang, Z. Yin, Q. Chen, *J. Phys. D. Appl. Phys.* **2000**, *33*, 912.
[26] J. Yang, X. Zhang, C. Wang, P. Sun, L. Wang, B. Xia, Y. Liu, *Solid State Sci.* **2012**, *14*, 139.
[27] R. Budakian, S. J. Putterman, *Phys. Rev. Lett.* **2000**, *85*, 1000.
[28] R. Eglītis, U. Joost, A. Zukuls, K. Rubenis, R. Ignatans, L. g. Avotiņa, L. Baumane, K. Smits, M. Hirsimaki, T. Kaambre, *ACS Appl. Mater. Interfaces* **2020**, *12*, 57609.
[29] a) Y. Ge, W. Li, J. Ren, Z. Shuai, *Phys. Rev. B* **2024**, *110*, 035201; b) Y. Liu, H. Wang, P. C. Sherrell, L. Liu, Y. Wang, J. Chen, *Adv. Sci.* **2021**, *8*, 2100669; c) Y. Pei, A. D. LaLonde, N. A. Heinz, X. Shi, S. Iwanaga, H. Wang, L. Chen, G. J. Snyder, *Adv. Mater* **2011**, *23*, 5674; d) M. Hong, W. Lyu, Y. Wang, J. Zou, Z.-G. Chen, *J. Am. Chem. Soc.* **2020**, *142*, 2672; e) J. F. Olorunyomi, B. P. Dyett, B. J. Murdoch, A. J. Ahmed, G. Rosengarten, R. A. Caruso, C. M. Doherty, X. Mulet, *Adv. Funct. Mater.* **2024**, 2403644.
[30] a) R. Xu, Q. Zhang, J. Y. Wang, D. Liu, J. Wang, Z. L. Wang, *Nano Energy* **2019**, *66*, 104185; b) Z. Zhang, D. Jiang, J. Zhao, G. Liu, T. Bu, C. Zhang, Z. L. Wang, *Adv. Energy Mater.* **2020**, *10*, 1903713; c) Y. Lu, S. Feng, R. Shen, Y. Xu, Z. Hao, Y. Yan, H. Zheng, X. Yu, Q. Gao, P. Zhang, *Research* **2019**, *2019*, 5832382.

This research was also supported by the Institute of Solid State Physics, University of Latvia, as the Center of Excellence has received funding from the European Union's Horizon 2020 Framework Program H2020-WIDESPREAD-01-2016-2017-TeamingPhase2 under grant agreement No. 739508, project CAMART2.